Supporting Information

An Allosteric Histidine Switch for Regulation of Intracellular Zinc(II) Fluctuation

Rongfeng Zhu[a,b,c,1], Yanqun Song[a,1], Haiping Liu[d,1], Yufei Yang[e], Shenlin Wang[e], Chengqi Yi[b,f], & Peng R. Chen[a,b,2]

[a]Synthetic and Functional Biomolecules Center, Beijing National Laboratory for Molecular Sciences, Key Laboratory of Bioorganic Chemistry and Molecular Engineering of Ministry of Education, College of Chemistry and Molecular Engineering, [b]Peking-Tsinghua Center for Life Sciences, and [c]Academy for Advanced Interdisciplinary Studies, Peking University, Beijing 100871, China. [d]Center for Chemical Biology, Tianjin Institute of Industrial Biotechnology, Chinese Academy of Sciences, Tianjin 300308, China. [e]Beijing NMR Center, College of Chemistry and Molecular Engineering, [f]School of Life Sciences, Peking University, Beijing 100871, China. [1]These authors contributed equally to the work. [2]To whom correspondence should be addressed. e-mail: pengchen@pku.edu.cn

➢ SI Text

➢ SI Figures

➢ SI Tables

SI Text

Structure of di-Zn(II)-ZitR^{WT} in complex with its operator DNA

In each asymmetric unit of the crystal, four identical protein-DNA complexes with two Zn(II) ions bound to each monomer protein were found and the structure showed a canonical MarR-type protein-DNA interaction with helices α4 and α4′ fitted into the major grooves of a B-form DNA **(Fig. S2A,B)**(1-6). Slight twisting and tightening up of the DNA-binding helices were found, with one asymmetric wing reconstructed in order to form an extra helix **(Fig. S2C,D)**. The dihedral angle formed by axes of helices α4 and α4' decreased 1.4 degree, and distance of helices α4 and α4' decreased from 30.1 Å to 28.0 Å **(Table S2)**. A lysine residue (K70) at helix α4 is buried deep in the major groove of DNA and forms hydrogen bonds with the N7 and O6 atoms of guanine 10 **(Fig. S2E,F)**. The functional role of the extra helix formed in the wing remains elusive, as the complexed DNA is only 16 bp in length and does not contain the minor groove that interacts with the winged β-sheet.

Structure of apo-ZitR^{C30AH42A}

We were unable to obtain the crystal structure of apo-ZitR protein when Zn(II) ions in both site 1 and site 2 were deprived, indicating that the protein may be very flexible in the absence of Zn(II). Thus we mutated the two Zn(II) binding residues, H42 in site 1 and C30 in site-2, to alanine. This double mutant ZitR^{C30AH42A} was successfully crystallized but later found to still contain one equivalent of non-specifically bound Zn(II) ion per monomer **(Fig. S3C and Table S1,S2)**. We then used excess EDTA to remove these non-specific Zn(II) ions and the structure of the resulting "apo" ZitR was determined at 2.2 Å resolution. This variant apo-ZitR^{C30AH42A} exhibited a similar conformation as that of Zn(II)$^{site\text{-}1}$-ZitR^{C30S} and ZitR^{C30AH42A} **(Fig. S3D-F and Table S1,S2)**. Superposition of the structures of di-Zn(II)-ZitR^{WT}, Zn(II)$^{site\text{-}1}$-ZitR^{C30S} and apo-ZitR^{C30AH42A} showed that whereas di-Zn(II)-ZitR^{WT} pre-locks the optimal conformation for DNA-binding, both Zn(II)$^{site\text{-}1}$-ZitR^{C30S} and apo-ZitR^{C30AH42A} showed large difference on the overall conformation. **(Fig. S3G)**.

ICP-MS of ZitR protein for metal-binding competition assay

We have performed ICP-MS to ensure that the our strategy to remove the Zn(II) ions in ZitR protein (EDTA treatment as indicated in Methods) is feasible for obtaining metal-free protein for titration experiments. As shown in **Table S2**, only less than 0.02 equivalent of Zn(II) remained in the EDTA-treated $ZitR^{WT}$ protein, which indicate that interactions of EDTA with ZitR protein is strong enough to allow remove of Zn(II) bound to ZitR protein. Meanwhile, the remained Zn(II) should have negligible effect in the competition assay.

The second coordinated Zn(II) in $ZitR^{E41A}$ structure

Site-1 residues in $ZitR^{E41A}$ remain the same with that in $ZitR^{WT}$. C30, E107, H111 and a water molecule together form a second Zn(II) coordinating site (site-2). Because we showed that $ZitR^{E41A}$ exhibited a similarly weakened DNA-binding affinity as that of $ZitR^{C30S}$ (whose site-2-bound Zn(II) is deprived), the function of $ZitR^{E41A}$ is very similar to $ZitR^{C30S}$ despite of having two Zn(II) coordinated (K_{DNA} for $ZitR^{E41A}$ and $ZitR^{C30S}$ are $5.4\pm0.1 \times 10^{-8}$ M and $2.0\pm0.2 \times 10^{-8}$ M respectively, both of which are different from $K_{DNA} = 2.6 \pm 0.4 \times 10^{-9}$ M for $ZitR^{WT}$). Unlike $ZitR^{C30S}$, the loop 1 in $ZitR^{E41A}$ stays in proximity with helix α5 due to the site-2's Zn(II) coordination residues E107 and H111. However, without E41 on helix α2, the second Zn(II) coordination cannot induce rearrangement of helix α2 as well as the DNA-binding motif to form a conformation optimal for DNA-binding. Therefore, H111 cannot work the same way as E41 even it is coordinated with Zn(II) in this $ZitR^{E41A}$ variant.

Comparison of hydrogen-bonding networks in contribution of ZitR's and AdcR's allosteric control of DNA recognition

AdcR possesses residues such as N38, Q40, and S74 that form an essential hydrogen-bonding network between the Zn(II)-binding sites and the DNA recognition helix (7). Residues N38 and S74 on AdcR are not conserved in ZitR while the conserved Q40 residue did not form hydrogen bonds with

other residues on helix α4 or with DNA bases **(Fig. S1C)**. In addition, more than half of the charged residues in ZitR's loop-1 region are not conserved in AdcR **(Fig. S1C)**.

MATERIALS AND METHODS

Reagents and equipments

Quin-2 (2-[2-(bis(carboxymethyl) amino - 5 - methylphenoxy)methyl] - 6 - methyl - 8 - [bis - (carboxymethyl)amino]quinoline) was purchased from Santa Cruz Biotechnology, Inc. Indo-1 (2-[4-[bis(carboxymethyl)amino]-3-[2-[2-[bis(carboxymethyl)amino]-5-methylphenoxy]ethoxy]phenyl]-1H-Indole-6-carboxylic acid, pentapotassium salt) was purchased from Invitrogen. δ-meH (3-methyl-histidine) and NaCl (≥99.999%, only for metal binding affinities measurements) were bought from Sigma-Aldrich Co. LLC. Water used for metal binding affinities measurements was bought from Hangzhou Wahaha Group Co., Ltd. All of the other chemicals were analytical grade or better. Protein purifications were carried out on ÄKTApurifier system (GE Healthcare). Oligonucleotides were all bought from Sangon Biotech (Shanghai) Co., Ltd.

Plasmids construction

The gene of ZitR (UniProt number: Q9CDU5) from strains IL1403 of *L. lactis* was subcloned into pET28b between sites NcoI and HindIII with stop codon before C-terminal his-tag. A methionine and a glycine residue were added to N-terminus of ZitR protein due to the start codon in the NcoI recognition sequence. Site-directed mutagenesis was applied to obtain ZitR mutants based on the QuickChange™ method developed by Stratagene (La Jolla, CA). Oligonucleotides used for the mutagenesis reactions are listed in **Table S4**. The *zitR-gfp* reporter plasmid was constructed by subcloning *zit* promoter from *L. lactis* IL1403 into pL(marO)-GFP plasmid between sites XhoI and KpnI, replacing the original marO

promoter (8). pBAD-ZitR was constructed by replacing the DiZPK-RS and Mb-tRNA-pyl in pSupAR plasmid with the gene of ZitR protein via Gibson Assembly (9, 10).

Protein expression and purification

pET28b-ZitR was transformed into *E. coli* BL21(DE3) strain. Then a single colony was collected and cultured overnight, followed by diluting into 1 L LB medium with the ratio of 1:100. For expression of ZitR mutant except ZitR$^{H42\delta meH}$, 1 mM IPTG (isopropyl β-D-1-thiogalactopyranoside) was added into LB medium after incubation at 37 °C for 3 h and the protein expression was induced at 30 °C for 3 h before harvest. Cell pellets were collected and resuspended in lysis buffer (20 mM Tris-HCl pH = 7.3). After sonicating on ice for 20 min, lysate of bacteria were centrifuged and the supernatant was loaded onto a 5-ml HiTrap Q FF column (GE Healthcare) before the standard segmented gradient procedure being applied to elute the protein (buffer A: 20 mM Tris-HCl, pH = 7.3; buffer B: 20 mM Tris-HCl, pH = 7.3, 1 M NaCl). The ZitR components were collected and further loaded onto a 5-ml HiTrap Heparin HP column (GE Healthcare). Linear gradient procedure (buffer A: 50 mM Tris-HCl, pH = 7.0, 1 mM $ZnCl_2$; buffer B: 50 mM Tris-HCl, pH = 7.0, 1 mM $ZnCl_2$, 2 M NaCl) was performed to separate ZitR protein. Finally, the protein sample was purified by size exclusion chromatography with HiLoad 16/60 Superdex 200 (GE Healthcare) equilibrated with 10 mM Tris-HCl, pH = 8.0, 100 mM NaCl, which can separate tetramer and dimer forms of ZitR. All the pH's of the buffers were measured at room temperature. The purifications were performed at 4 °C.

ZitR$^{H42\delta meH}$ was expressed in *E. coli* DH10B strain following previously reported procedure (11). Purification of ZitR$^{H42\delta meH}$ protein was generally performed with the same method as described above, with an additional purification with a Mono Q 5/50 GL column (GE Healthcare) before size exclusion chromatography. Linear gradient procedure (buffer A: 50 mM Tris-HCl, pH = 6.7; buffer B: 50 mM Tris-HCl, pH = 6.7, 1 M NaCl) was performed to separate ZitR protein. An LC/MS analysis of purified ZitR$^{H42\delta meH}$ was performed using a Waters ACQUITY UPLC I-Class SQD 2 MS spectrometer with electrospray ionization (ESI).

ICP-MS analysis

Generally purified ZitR variants were concentrated to 5~10 mg/mL in 10 mM Tris-HCl, pH = 8.0, 100 mM NaCl. 100 μL samples were submitted to analyze the total weight of Zn by 8800 Triple Quadrupole ICP-MS (Agilent Technologies) in China National Food and Safety Supervision and Inspection Center. The Zn/protein molar ratios were calculated and shown in **Table S2**. For EDTA-treated ZitR protein, the protein was 1 mg/mL in 25 mM Tris-HCl, pH = 8.0, 250 mM NaCl, and 100 μL samples were submitted to analyze.

Crystallization

All the crystallization experiments in this study were performed with sitting-drop vapor diffusion at 20 °C. Crystals of zinc-bound ZitR and variants were screened with kits from Hampton Research (Index, Crystal Screen, PEGRx 1, PEGRx 2, PEG/Ion Screen, PEG/Ion 2 Screen). 1.5 μl ZitR protein solution (~15 mg/mL in 10 mM Tris-HCl, pH = 8.0, 100 mM NaCl) and 1.5 μl reservoir solution were mixed. Single crystals could be observed after 24 hours. To obtain crystal of apo-ZitR^{C30AH42A}, 10 mM EDTA was added into the droplets containing crystals of ZitR^{C30AH42A} and the soaked crystals were collected after 24 h. For crystallization of ZitR-DNA complex, the solution of ZitR variants (5 mg/mL in 10 mM Tris-HCl, pH = 6.5) was mixed with double-stranded DNA (Protein:DNA ratio = 1:1.5 or 1:2) for at least 30 min at 4 °C. Then the mixtures were screened with reservoir solutions containing 100 mM NaCl, 50 mM $MgCl_2$, 100 mM sodium cacodylate of various pH (5.5-6.5), and different concentrations of PEG 8000 or PEG 4000 (w/v 12%-24%). DNA of various sequence were attempted in crystallization, which have different length from 12 bp to 20 bp and contain the imperfect TTA ACY RGT TAA palindromes from the native *zit* promoter sequence (12). The sequence of DNA generating crystals of ZitR-DNA complex that has the best diffraction was found to be palindromic blunt-ended 16 bp 5'-TGT TAA CTA GTT AAC A-3'. The growing conditions for crystals with the best diffraction quality are listed in **Table S3**.

X-ray data collection and structure determination.

Crystals were washed with cryoprotectant freshly made by mixing reservoir solution with 90% glycerol in 7:2 ratio, and then flash frozen in liquid nitrogen prior to X-ray diffraction. Diffraction data sets of di-Zn(II)-ZitR^{WT}, Zn(II)$^{site-1}$-ZitR^{C30S}, Zn(II)$^{site-1}$-ZitR^{C30S}-DNA, ZitR^{C30AH42A} and apo-ZitR^{C30AH42A} were collected by beamlines of BL17U1 at Shanghai Synchrotron Radiation Facility (SSRF) with wavelength at 0.9785 Å for di-Zn(II)-ZitR^{WT} and Zn(II)$^{site-1}$-ZitR^{C30S}, 0.9792 Å for Zn(II)$^{site-1}$-ZitR^{C30S}-DNA and ZitR^{C30AH42A}, and 0.9793 Å for apo-ZitR^{C30AH42A}, respectively. Diffraction data sets of di-Zn(II)-ZitR^{WT}-DNA were collected by beamlines of BL19U1 at SSRF with wavelength at 0.9786 Å. Diffraction data sets of Zn(II)-ZitR^{E41A} was collected by beamlines of 1W2B at Beijing Synchrotron Radiation Facility (BSRF) with wavelength at 0.9795 Å. The collected data sets were processed with HKL2000 or HKL3000 (13), and structures were solved via molecular replacement with programs Phaser (14) and MOLREP (15) in CCP4 package (16). Structures of AdcR (Protein Data Bank code 3TGN) and SlyA-DNA complex (Protein Data Bank code 3Q5F) are used as search models for ZitR protein and ZitR-DNA complex respectively. Refinement was performed by programs REFMAC5 (17), Phenix (18) and COOT (19). The Ramachandran plot given by MolProbity (20) showed that in every structure, proportions of residues in the disallowed region were 0.7%, 0%, 0%, 1.1%, 0%, 0.3%, 0% for di-Zn(II)-ZitR^{WT}, Zn(II)$^{site-1}$-ZitR^{C30S}, di-Zn(II)-ZitR^{WT}-DNA, Zn(II)$^{site-1}$-ZitR^{C30S}-DNA, Zn(II)-ZitR^{E41A}, ZitR^{C30AH42A} and apo-ZitR^{C30AH42A}, respectively. Protein sequence alignment was performed by ClustalW (21-23). Electrostatic calculations were performed by PDB2PQR (24, 25) and APBS (26). PyMOL was used to generate all of the figures. Summary of the data statistics is listed in **Table S1**.

Metal binding affinities measured by competition with quin-2/indo-1

ZitR protein was treated with 10 mM EDTA and desalted by HiTrap Desalting columns (GE Healthcare) to remove metal ions. This metal-free ZitR protein was diluted to stated concentration in

120 μL buffer (25 mM Tris-HCl, pH = 8.0 or 25 mM Bis-tris-HCl, pH = 6.0; 250 mM NaCl) containing variable quin-2 or indo-1 followed by addition of different concentrations of $ZnCl_2$ solution. The mixtures were equilibrated at room temperature for 30 min and their optical spectra were subsequently recorded from 240 nm to 440 nm for quin-2 and from 270 nm to 500 nm for indo-1 by U-3900 spectrophotometer (Hitachi). The change of absorption at 265/365 nm caused by the addition of different amounts of Zn(II) revealed the extent of competition between protein and quin-2/indo-1, respectively. These data were fitted by Dynafit (27) using a competitive binding model to determine the zinc binding affinity of site 1 for ZitR variants. The affinity of Zn(II) to quin-2 was 3.7×10^{-12} M and indo-1 was 1.6×10^{-10} M according to previously reported result (28, 29). Reported dissociation constants are mean ± SEM of three independent experiments. An example of Dynafit script is shown below:

```
[task]
        task = fit
        data = equilibria
[mechanism]
        P + Zn <==> P.Zn            :          Kdp     dissociation
        Q + Zn <==> Q.Zn            :          Kdq     dissociation
[constants] ; micromolar
        Kdq = 0.0000037    ; KZn of quin-2
        Kdp = 0.000007 ?    ; KZn of ZitR monomer protein, estimate based on titration
[concentrations] ; micromolar
        P = 36.2 ; protein
        Q = 19.9 ; quin-2
[responses]
        Q = 0.03402 ; initial absorbance at 265 nm divided by quin-2 concentration
        Q.Zn = 0.00799 ; final absorbance at 265 nm divided by quin-2 concentration
```

[data]

variable Zn

file ./data/C30S.txt

[output]

directory ./output/fit-C30S

[end]

In the script, protein concentration was calculated by absorbance at 280 nm with a coeffiecient of 6970 $M^{-1}\cdot cm^{-1}$, quin-2 concentration was determined by the coeffiecient change at 265 nm ($\Delta\varepsilon_{265nm}$ = -2.6×10^4 $M^{-1}\cdot cm^{-1}$) (29). For measurement with indo-1, the parameter Kdq was replaced by K_{Zn} of indo-1 (0.00016), indo-1 concentration was determined by the coeffiecient change at 365 nm ($\Delta\varepsilon_{365nm}$ = -2.1×10^4 $M^{-1}\cdot cm^{-1}$) (29). The parameters Q and Q.Zn were calculated by initial and final absorbances at 365 nm divided by indo-1 concentration, respectively.

Fluorescence anisotropy

A 28 mer DNA whose sequence form native *zit* promoter with TET (Tetrachlorofluorescein) dye labeled at 3' terminal (5'-AAA TAA TGT TAA CTG GTT GAC ATT ATT T-TET-3') was annealed with its complementary sequence before use (12). The double stranded DNA (dsDNA) was diluted to 10 nM in 500 μL buffer (50 mM Tris-HCl, pH = 8.0, 200 mM NaCl, 1 μM $ZnCl_2$, 0.005% Tween-20) in cuvette. Then different amounts of zinc-bound ZitR protein were titrated into the DNA solution and for each aliquot of added protein, 50 data points of anisotropy were collected in a 5 min period and their average value was used for determining the binding affinity. Measurements of fluorescent anisotropy were applied on Cary Eclipse Fluorescence Spectrophotometer (Agilent Technologies). The excitation wavelength was set at 520 nm and the emission wavelength was set at 550 nm with both slits set at 10 nm. The final data was analyzed and fitted by Dynafit (27) assuming a one-to-one binding model to determine the binding affinity of ZitR dimer protein to DNA. The mean initial anisotropy value for the free DNA is 0.159, and the maximum anisotropy changes are 0.028, 0.027, 0.029, 0.029, 0.033, 0.031

for $ZitR^{WT}$ measured with 10 nM DNA, $ZitR^{WT}$ measured with 2 nM DNA, $ZitR^{C30S}$, $ZitR^{E41A}$, $ZitR^{C30AH42A}$, $ZitR^{H42\delta meH}$ respectively. Reported dissociation constants are mean ± SEM of three independent experiments. An example of Dynafit script is shown below:

```
[task]
    task = fit
    data = equilibria
[mechanism]
    P + D <==> P.D        :        Kdp    dissociation
[constants] ; nanomolar
    Kdp = 1 ?    ; KDNA of protein, estimate based on titration
[responses]
    intensive
    D = 0.162 ?    ; initial anisotropy
    P.D = 0.190 ?    ; final anisotropy
[data]
    variable P, D ; P stands for ZitR dimer protein, and D stands for double-stranded DNA
    plot titration
    file ./data /WT.txt
[output]
    directory ./output/fit-WT
[end]
```

SPR analysis of protein–DNA interactions

The surface plasmon resonance method was performed on a Biacore T200 (GE Healthcare). 3'-biotinylated DNA fragments corresponding to ZitR binding regions (5'-AAA TAA TGT TAA CTG

GTT GAC ATT ATT T-biotin-3') were annealed to its complementary oligonucleotides (12). The biotinylated dsDNA fragments at 2 nM in running buffer (25 mM Tris-HCl, pH = 8.0, 400 mM NaCl, 1 μM $ZnCl_2$, 0.002% Tween-20) were passed at a flow rate of 1 μl/min over the streptavidin-coated sensor chip (SA sensor chip) and approximately 50 resonance units (RU) were captured. The subsequent binding assays were carried out in the same buffer. Samples with various concentrations of $ZitR^{WT}$ or $ZitR^{C30S}$ dimer proteins were injected for 210 s at a flow rate of 100 μl/min at 25 °C, followed by injection of blank buffer for 350 s. The chip surface was regenerated by passing 1 M NaCl for 60 s. Kinetic analyses of sensorgrams were performed with Biacore Evaluation Software. Reported rate constants and affinity values are mean ± SEM of three independent experiments.

Flow cytometry

An overnight *E. coli* BW25113 culture harboring both the *zitR-gfp* reporter plasmid and the pBAD-ZitR plasmid was inoculated (1:100) in LB medium and grown to an OD_{600nm} of 0.6. Arabinose with 0.3 mM in final concentration was added to induce expression of ZitR protein. After 3 h induction, the culture was diluted (1:100) in LB medium with 0.03 mM arabinose added and incubated for 1 h. Bacterial cells were next treated with or without 100 μM $ZnCl_2$, 1 h before being analyzed by flow cytometry.

REFERENCE

1. Perera IC & Grove A (2010) Molecular mechanisms of ligand-mediated attenuation of DNA binding by MarR family transcriptional regulators. *J Mol Cell Biol* 2(5):243-254.
2. Wilkinson SP & Grove A (2006) Ligand-responsive transcriptional regulation by members of the MarR family of winged helix proteins. *Curr Issues Mol Biol* 8(1):51.
3. Birukou I, Seo SM, Schindler BD, Kaatz GW, & Brennan RG (2014) Structural mechanism of transcription regulation of the *Staphylococcus aureus* multidrug efflux operon *mepRA* by the MarR family repressor MepR. *Nucleic Acids Res* 42(4):2774-2788.

4. Dolan KT, Duguid EM, & He C (2011) Crystal structures of SlyA protein, a master virulence regulator of *Salmonella*, in free and DNA-bound states. *J Biol Chem* 286(25):22178-22185.
5. Hong M, Fuangthong M, Helmann JD, & Brennan RG (2005) Structure of an OhrR-*ohrA* operator complex reveals the DNA binding mechanism of the MarR family. *Mol Cell* 20(1):131-141.
6. Zhu R*, et al.* (2017) Structural characterization of the DNA-binding mechanism underlying the copper(II)-sensing MarR transcriptional regulator. *J Biol Inorg Chem* 22(5):685-693.
7. Guerra AJ, Dann CE, & Giedroc DP (2011) Crystal structure of the zinc-dependent MarR family transcriptional regulator AdcR in the Zn(II)-bound state. *J Am Chem Soc* 133(49):19614-19617.
8. Hao Z*, et al.* (2014) The multiple antibiotic resistance regulator MarR is a copper sensor in *Escherichia coli*. *Nat Chem Biol* 10(1):21-28.
9. Gibson DG*, et al.* (2009) Enzymatic assembly of DNA molecules up to several hundred kilobases. *Nat Methods* 6(5):343-345.
10. Zhang M*, et al.* (2011) A genetically incorporated crosslinker reveals chaperone cooperation in acid resistance. *Nat Chem Biol* 7(10):671-677.
11. Xiao H*, et al.* (2014) Genetic incorporation of histidine derivatives using an engineered pyrrolysyl-tRNA synthetase. *ACS Chem Biol* 9(5):1092-1096.
12. Llull D*, et al.* (2011) *Lactococcus lactis* ZitR is a zinc-responsive repressor active in the presence of low, nontoxic zinc concentrations *in vivo*. *J Bacteriol* 193(8):1919-1929.
13. Otwinowski Z & Minor W (1997) Processing of X-ray diffraction data collected in oscillation mode. *Methods Enzymol*, eds Carter CW, Jr. & Sweet RM (Academic Press, New York), Vol 276: Macromolecular Crystallography, part A, pp 307-326.
14. McCoy AJ*, et al.* (2007) Phaser crystallographic software. *J Appl Crystallogr* 40(4):658-674.
15. Vagin A & Teplyakov A (1997) MOLREP: an automated program for molecular replacement. *J Appl Crystallogr* 30(6):1022-1025.
16. Winn MD*, et al.* (2011) Overview of the CCP4 suite and current developments. *Acta Crystallogr Sect D Biol Crystallogr* 67(4):235-242.
17. Murshudov GN, Vagin AA, & Dodson EJ (1997) Refinement of Macromolecular Structures by the Maximum-Likelihood Method. *Acta Crystallogr Sect D Biol Crystallogr* 53(3):240-255.
18. Adams PD*, et al.* (2010) PHENIX: a comprehensive Python-based system for macromolecular structure solution. *Acta Crystallogr Sect D Biol Crystallogr* 66(2):213-221.
19. Emsley P, Lohkamp B, Scott WG, & Cowtan K (2010) Features and development of Coot. *Acta Crystallogr Sect D Biol Crystallogr* 66(4):486-501.
20. Chen VB*, et al.* (2010) MolProbity: all-atom structure validation for macromolecular crystallography. *Acta Crystallogr Sect D Biol Crystallogr* 66(1):12-21.
21. Larkin MA*, et al.* (2007) Clustal W and Clustal X version 2.0. *Bioinformatics* 23(21):2947-2948.
22. Goujon M*, et al.* (2010) A new bioinformatics analysis tools framework at EMBL–EBI. *Nucleic Acids Res* 38(suppl 2):W695-W699.

23. McWilliam H*, et al.* (2013) Analysis tool web services from the EMBL-EBI. *Nucleic Acids Res* 41(W1):W597-W600.
24. Dolinsky TJ, Nielsen JE, McCammon JA, & Baker NA (2004) PDB2PQR: an automated pipeline for the setup of Poisson–Boltzmann electrostatics calculations. *Nucleic Acids Res* 32(suppl 2):W665-W667.
25. Dolinsky TJ*, et al.* (2007) PDB2PQR: expanding and upgrading automated preparation of biomolecular structures for molecular simulations. *Nucleic Acids Res* 35(suppl 2):W522-W525.
26. Baker NA, Sept D, Joseph S, Holst MJ, & McCammon JA (2001) Electrostatics of nanosystems: application to microtubules and the ribosome. *Proc Natl Acad Sci U S A* 98(18):10037-10041.
27. Kuzmič P (1996) Program DYNAFIT for the analysis of enzyme kinetic data: application to HIV proteinase. *Anal Biochem* 237(2):260-273.
28. Reyes-Caballero H*, et al.* (2010) The metalloregulatory zinc site in *Streptococcus pneumoniae* AdcR, a zinc-activated MarR family repressor. *J Mol Biol* 403(2):197-216.
29. Jefferson JR, Hunt JB, & Ginsburg A (1990) Characterization of indo-1 and quin-2 as spectroscopic probes for Zn2+-protein interactions. *Anal Biochem* 187(2):328-336.

SI FIGURES

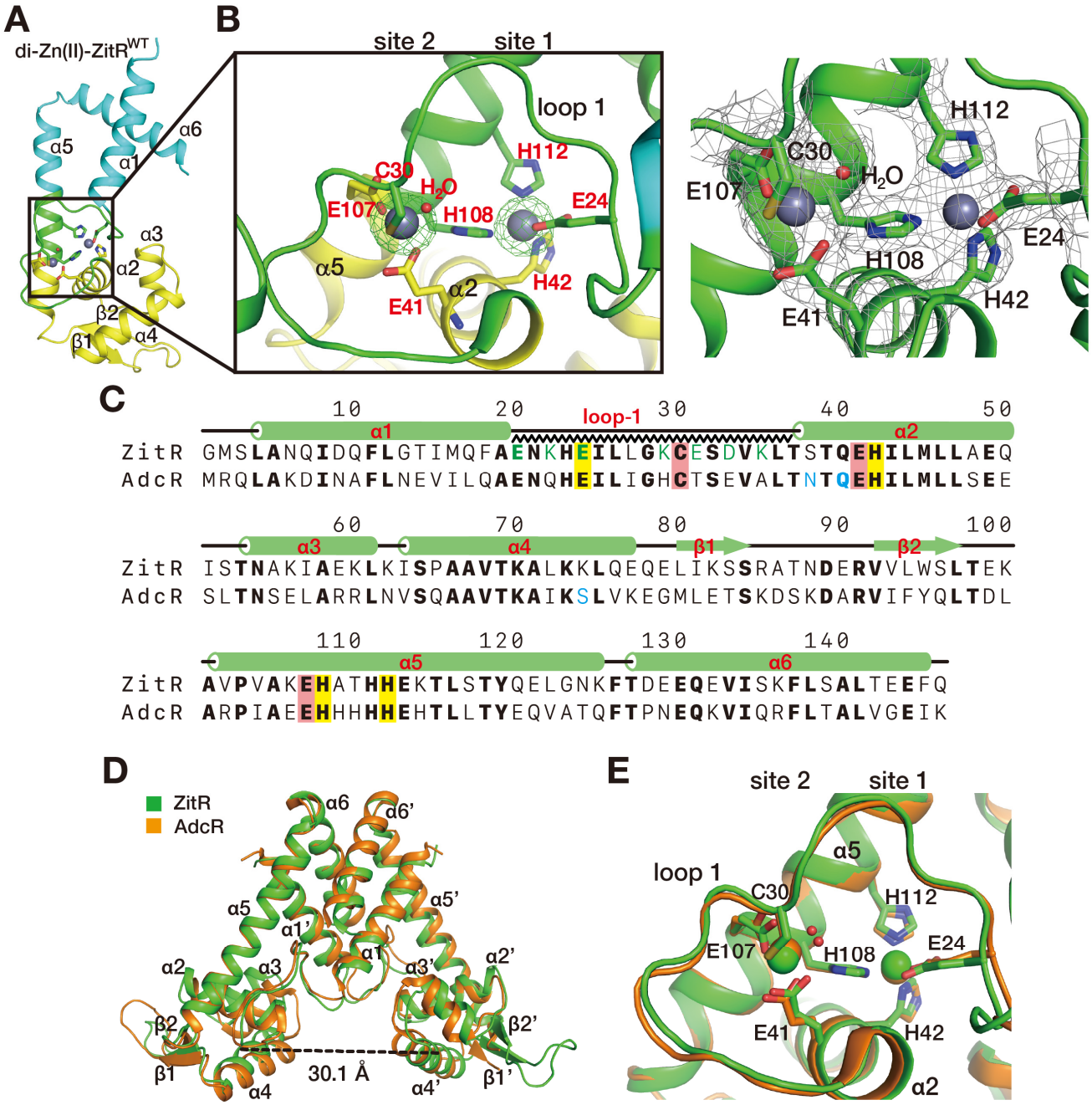

Figure S1. Crystal structure of di-Zn(II)-ZitR^{WT} protein and comparison with di-Zn(II)-AdcR^{WT}. **(A)** Monomeric representation of di-Zn(II)-ZitR^{WT}. The dimerization domain (residues 1-19 and 116-146), winged-HTH DNA binding domain (residues 39-107) and the connection regions (residues 20-38 and 108-115) are colored in cyan, yellow and green, respectively. **(B)** Close up view of the two

zinc-binding sites of di-Zn(II)-ZitR^{WT}. Site-1($K_d \approx 10^{-13}\,M^{-1}$) has a higher Zn(II)-affinity than site 2 ($K_d \approx 10^{-9}\,M^{-1}$). F_o-F_c omit electron density map of the bound Zn(II) ions are shown, with the map contoured at 3.0σ and displayed as green mesh. $2F_o$-F_c electron density map contoured at 1.0σ is displayed as gray mesh. **(C)** Protein sequence alignment of ZitR and AdcR (The sequence are numbered according to AdcR). The alignment exhibited 48% sequence identity. Residues involved in zinc binding are marked in yellow (site-1: E24, H42, H108, H112) and pink (site-2: C30, E41, E107) box respectively. Charged residues in ZitR's loop-1 region are colored in green. Resides N38, Q40, and S74 in AdcR that are involved in hydrogen bond networks for DNA interactions are colored in blue. **(D)** Structural superposition of the entire di-Zn(II)-ZitR^{WT} and di-Zn(II)-AdcR^{WT} proteins (rmsd = 1.50 Å for 247 Cα atoms). The distance between helix α4 and α4' in dimeric di-Zn(II)-ZitR^{WT} was measured to be 30.1 Å. **(E)** Structural comparison of the zinc-binding sites (site 1 and site-2) between di-Zn(II)-ZitR^{WT} (green) and di-Zn(II)-AdcR^{WT} (orange).

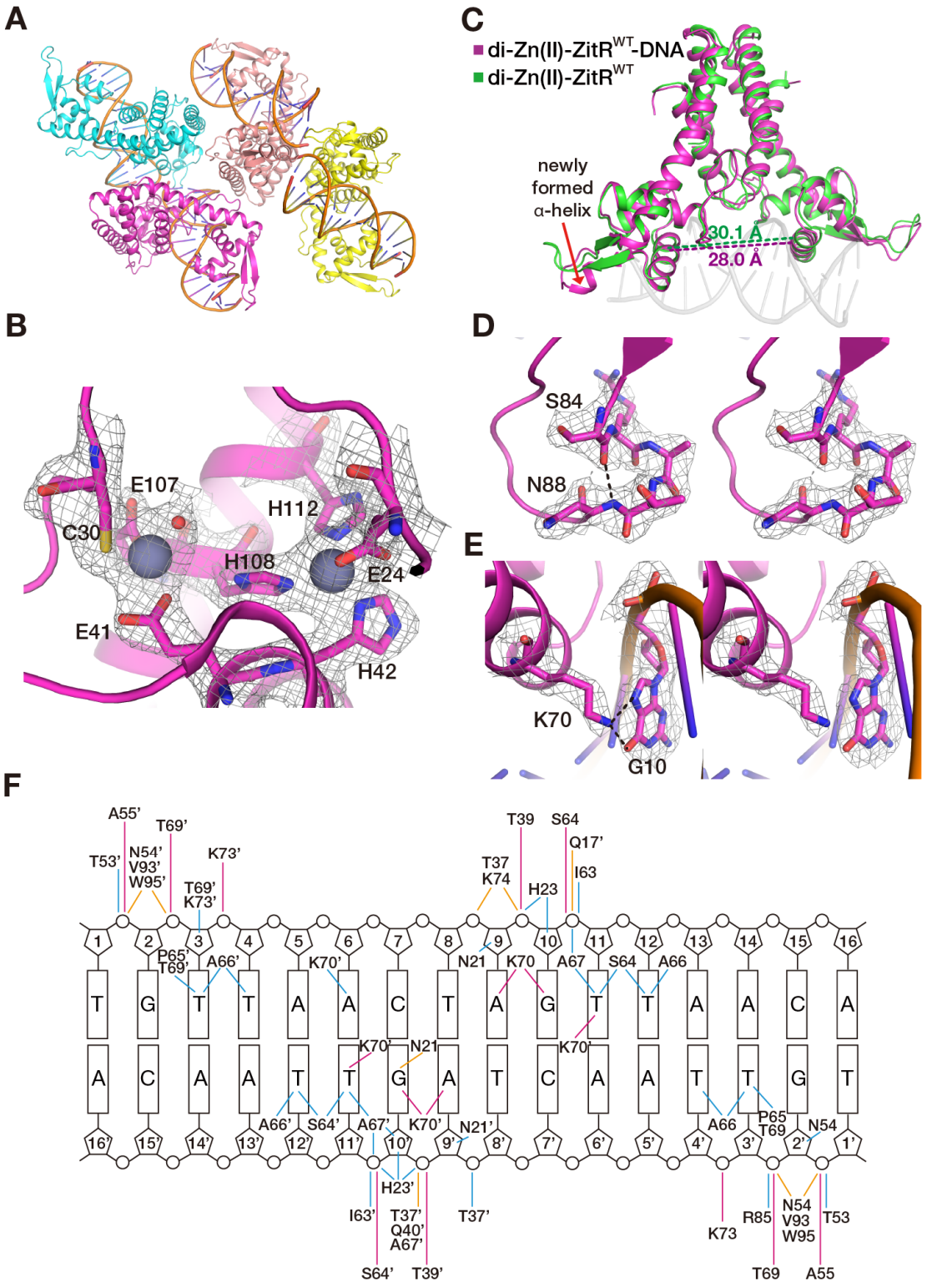

Figure S2. Crystal structure of di-Zn(II)-ZitR^{WT}-DNA complex. (A) Four separate complexes were contained in each asymmetric unit and colored differently. **(B)** Close up view of the two zinc-binding

sites of di-Zn(II)-ZitR^{WT}-DNA. 2F_o-F_c electron density map contoured at 1.0σ is shown as gray mesh. **(C)** Structural comparison between di-Zn(II)-ZitR^{WT} and di-Zn(II)-ZitR^{WT}-DNA complex (rmsd = 0.85 Å for 275 Cα atoms). Distances between helices α4 and α4' in dimeric di-Zn(II)-ZitR^{WT} and di-Zn(II)-ZitR^{WT}-DNA were labeled with dashed lines. **(D)** Stereo view of newly formed α helix in the β-hairpin region. Black dashed line indicates the main-chain i to i+4 hydrogen bond between residues S84 and N88. **(E)** Stereo view of residue K70 of ZitR protein interacting with G10 in the cognate DNA. 2F_o-F_c electron density map contoured at 1.0σ is shown as gray mesh in **(D,E)**. **(F)** Schematic representation of interactions between di-Zn(II)-ZitR^{WT} protein and DNA in the structure. Magenta lines indicate direct hydrogen bonds and orange lines indicate water-mediated contacts. Cyan lines indicate van der Waals interactions.

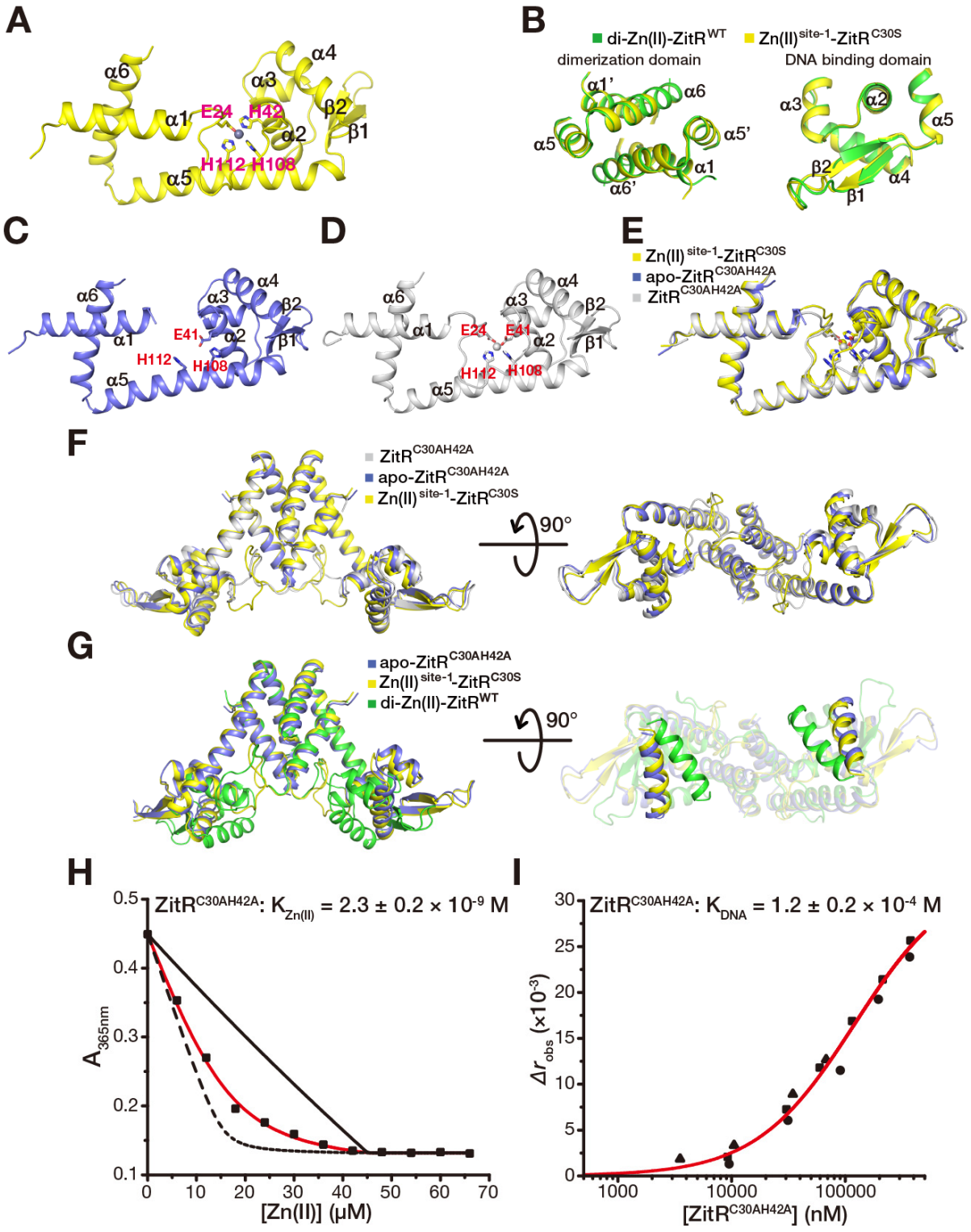

Figure S3. Structural and biochemical characterization of Zn(II)$^{site\text{-}1}$-ZitR^{C30S} and ZitR^{C30AH42A}. (A) Structure of monomeric Zn(II)$^{site\text{-}1}$-ZitR^{C30S} with the side-chains of site-1 residues shown and labeled. **(B)**

Superposition of the dimerization domain and the winged-HTH DNA binding domain of di-Zn(II)-ZitR^{WT} (green) and Zn(II)$^{site\text{-}1}$-ZitR^{C30S} (yellow). Rmsd = 0.39 Å for 85 Cα atoms in the dimerization domain and 0.45 Å for 65 Cα atoms in the DNA binding domain. **(C)** Structure of monomeric ZitR^{C30AH42A}. Side-chains of site-1 residues are shown and labeled. This structure still contains one equivalent of non-specifically bound Zn(II) ion per monomer. **(D)** Structure of monomeric apo-ZitR^{C30AH42A}. This structure was obtained by soaking crystals of ZitR^{C30AH42A} with EDTA. **(E)** Superpositions of monomeric Zn(II)$^{site\text{-}1}$-ZitR^{C30S}, ZitR^{C30AH42A}, and apo-ZitR^{C30AH42A}. Similar conformations were observed among these three protein (rmsd of ZitR^{C30AH42A} with Zn(II)$^{site\text{-}1}$-ZitR^{C30S}: 1.18 Å for 128 Cα atoms; rmsd of apo-ZitR^{C30AH42A} with Zn(II)$^{site\text{-}1}$-ZitR^{C30S}: 0.74 Å for 120 Cα atoms). **(F)** Superpositions of dimeric Zn(II)$^{site\text{-}1}$-ZitR^{C30S}, ZitR^{C30AH42A} and apo-ZitR^{C30AH42A}. Dimeric structures of these ZitR variants also utilize similar overall conformations (rmsd of ZitR^{C30AH42A} with Zn(II)$^{site\text{-}1}$-ZitR^{C30S}: 1.34 Å for 249 Cα atoms; rmsd of apo-ZitR^{C30AH42A} with Zn(II)$^{site\text{-}1}$-ZitR^{C30S}: 1.17 Å for 260 Cα atoms). **(G)** Superpositions of dimeric di-Zn(II)-ZitR^{WT}, Zn(II)$^{site\text{-}1}$-ZitR^{C30S} and apo-ZitR^{C30AH42A}. Zn(II)$^{site\text{-}1}$-ZitR^{C30S} adopts a similar non-DNA-binding conformation as apo-ZitR^{C30AH42A} while di-Zn(II)-ZitR^{WT} has large difference (rmsd between di-Zn(II)-ZitR^{WT} and apo-ZitR^{C30AH42A}: 4.20 Å for 210 Cα atoms; rmsd between Zn(II)$^{site\text{-}1}$-ZitR^{C30S} and apo-ZitR^{C30AH42A}: 1.17 Å for 260 Cα atoms). **(H)** Representative binding isotherms of titrating Zn(II) into a mixture of 30.0 μM ZitR^{C30AH42A} monomer and 15.1 μM indo-1. The red solid lines are fitting to a model for 1:1 stoichiometric binding while the black solid and dashed lines are simulated curves with Zn(II) affinities of ZitR proteins 10-fold tighter and weaker than the fitted value, respectively. **(I)** Binding isotherms of titrating ZitR^{C30AH42A} into the fluorescently labeled *zit* promoter DNA. The *x* axes is plotted on a logarithmic scale. The red solid lines are simulated curves of the mean K_{DNA} values in a 1:1 ZitR dimer:DNA binding model. Indicated affinity values are mean ± SEM of three independent experiments (different symbol shapes).

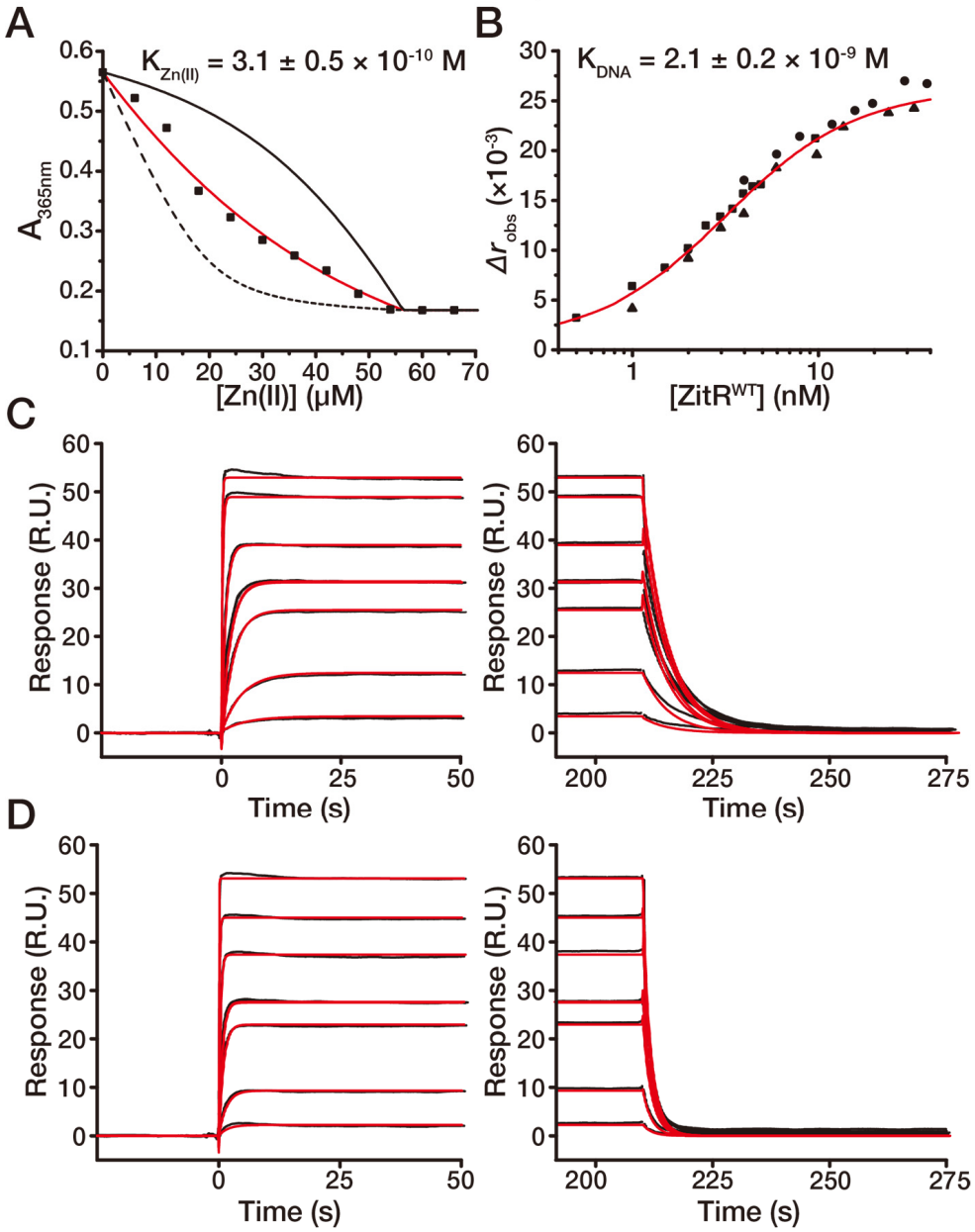

Figure S4. Supplementary biochemical characterization of ZitR^{WT}. (A) Representative binding isotherms of titrating Zn(II) into a mixture of 37.5 μM ZitR^{WT} monomer and 18.9 μM indo-1. The red solid lines are fitting to a model for 1:1 stoichiometric binding while the black solid and dashed lines are simulated curves with Zn(II) affinities of ZitR proteins 10-fold tighter and weaker than the fitted value, respectively. **(B)** Binding isotherms of titrating ZitR^{WT} into low concentration of the fluorescently labeled *zit* promoter DNA. 2 nM DNA was utilized in the experiment to deal with

potential issue of local minima. Slight difference of apparent K_{DNA} under this condition with that of 10 nM DNA ($2.1 \pm 0.2 \times 10^{-9}$ M with 2 nM DNA versus $2.6 \pm 0.4 \times 10^{-9}$ M with 10 nM DNA) indicates that measurements with 10 nM DNA is reliable. The *x* axes is plotted on a logarithmic scale. The red solid lines are simulated curves of the mean apparent K_{DNA} values in a 1:1 ZitR dimer:DNA binding model. Indicated affinity values are mean ± SEM of three independent experiments (different symbol shapes). **(C, D)** Expanded view of the SPR sensorgrams of di-Zn(II)-ZitR^{WT} **(C)** and Zn(II)$^{site\text{-}1}$-ZitR^{C30S} **(D)** in the **Fig.2E, F** of the main text.

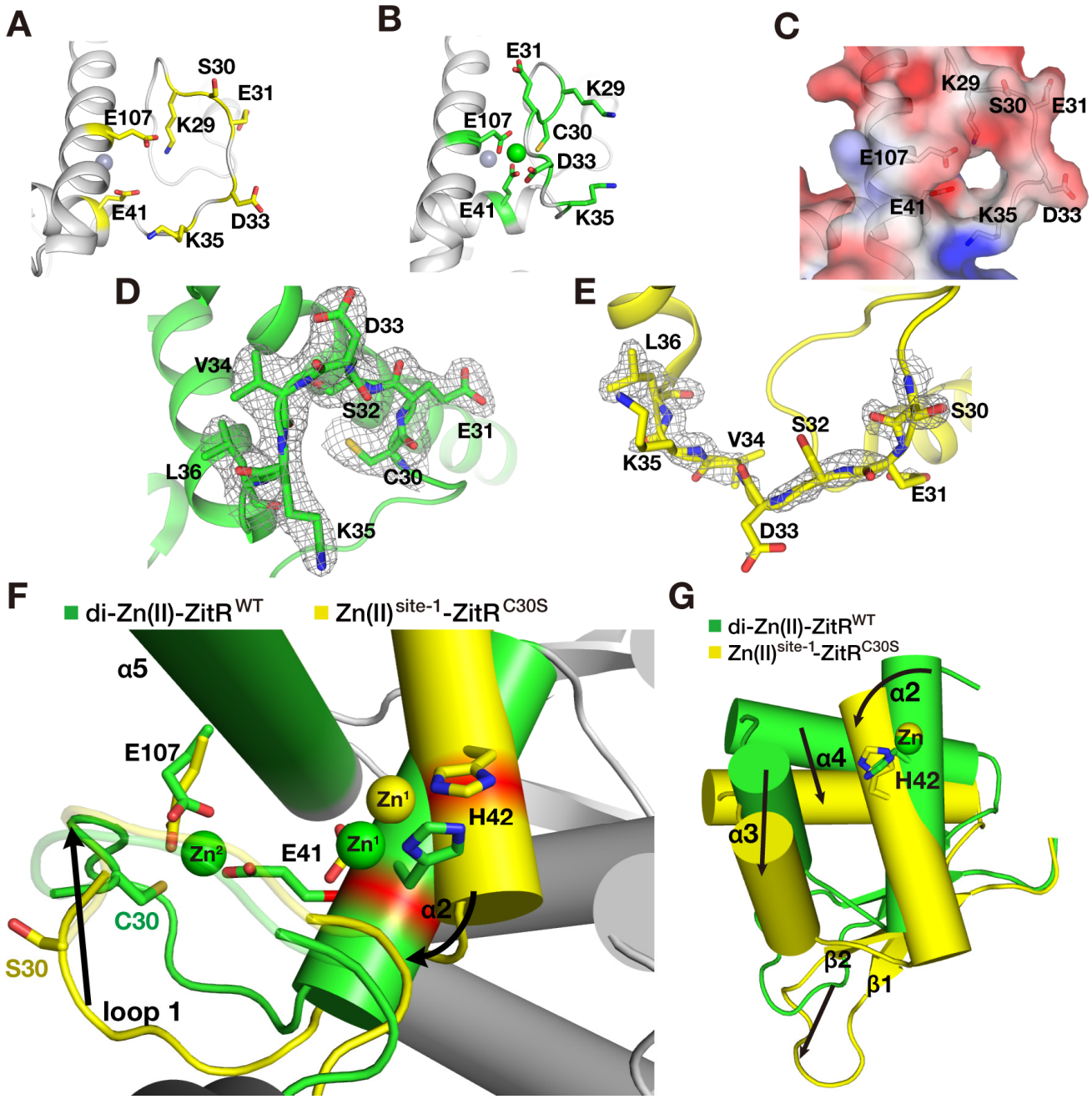

Figure S5. Electrostatic repulsions and correlated conformational changes induced by Zn(II)-binding in site-2. **(A, B)** Orientation of site-2 residues (C30, E41, E107) and the four charged residues from loop 1 (K29, E31, D33, K35) in $Zn(II)^{site\text{-}1}$-$ZitR^{C30S}$ **(A)** and di-Zn(II)-$ZitR^{WT}$ **(B)**. **(C)** Molecular electrostatic potential surface of site-2 cavity in $Zn(II)^{site\text{-}1}$-$ZitR^{C30S}$. Red and blue surfaces represent negative and positive electrostatic potentials respectively, scaling from −3.0 kT/e to +3.0 kT/e.

Side-chains of residues are shown as sticks and labeled. **(D,E)** $2F_o$-F_c electron density map of residues 30-36 in loop 1 of di-Zn(II)-ZitR^{WT} **(D)** and Zn(II)$^{site\text{-}1}$-ZitR^{C30S} **(E)**. The maps are contoured at 1.0σ and shown as gray mesh. **(F)** Conformational changes upon Zn(II)-binding in site-2. Coordination of Zn(II) ion at site 2 brings loop 1 to close proximity to helix α5, which further triggers a structural rearrangement of helix α2. Structures of Zn(II)$^{site\text{-}1}$-ZitR^{C30S} (yellow) and di-Zn(II)-ZitR^{WT} (green) are superimposed at helix α5. Cα atom of E41 on helix α2 is colored with red for clarity. Zn^1 and Zn^2 in the figure refer to Zn(II) ions at site 1 and site-2, respectively. Black arrows indicate movement of loop 1 and helix α2 upon Zn(II) coordination at site-2. **(G)** Rearrangement of the DNA binding motif in the site-2-induced conformational change. Due to the rigid conformation of wHTH motif, rotation of helix α2 induces translation of helices α3, α4 and the winged β-sheets.

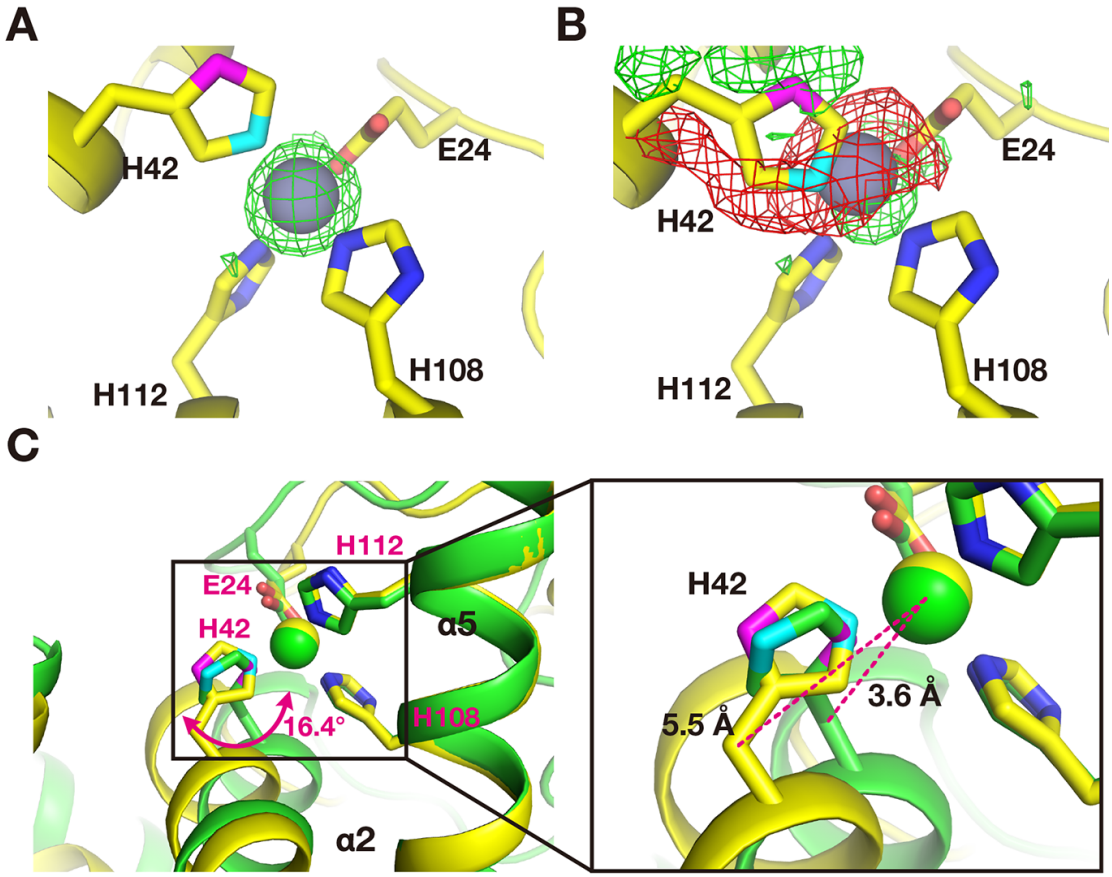

Figure S6. Histidine-switch of H42 residue in site-1. **(A, B)** F_o-F_c omit electron density map of site 1 modeled with Nε2-coordinating **(A)** and Nδ1-coordinating **(B)** H42 in Zn(II)$^{site\text{-}1}$-ZitR^{C30S}, respectively. The positive and negative density around H42 together with the unfavorable geometry of H42 in **(B)**, which are absent in **(A)**, indicate errors in the model of **(B)** and that Nε2 but not Nδ1 is used for coordination of Zn(II) ion (gray sphere) in site 1 of Zn(II)$^{site\text{-}1}$-ZitR^{C30S}. Maps are contoured at 3.0σ (green) and -3.0σ (red) respectively. **(C)** Superposition of di-Zn(II)-ZitR^{WT} (green) and Zn(II)$^{site\text{-}1}$-ZitR^{C30S} (yellow) at helix α5. The Zn(II)-coordination atom on H42 is switched from Nδ1 (di-Zn(II)-ZitR^{WT}) to Nε2 (Zn(II)$^{site\text{-}1}$-ZitR^{C30S}). Helix α2 is rotated by 16.4°, which is likely caused by Zn(II)-binding in site 2 and further decreases the distance between Cβ atom of H42 and Zn(II) ion from 5.5 Å to 3.6 Å (in the zoomed rectangle). Nδ1 and Nε2 of H42 are shown as magenta and cyan respectively for clarity in all panels.

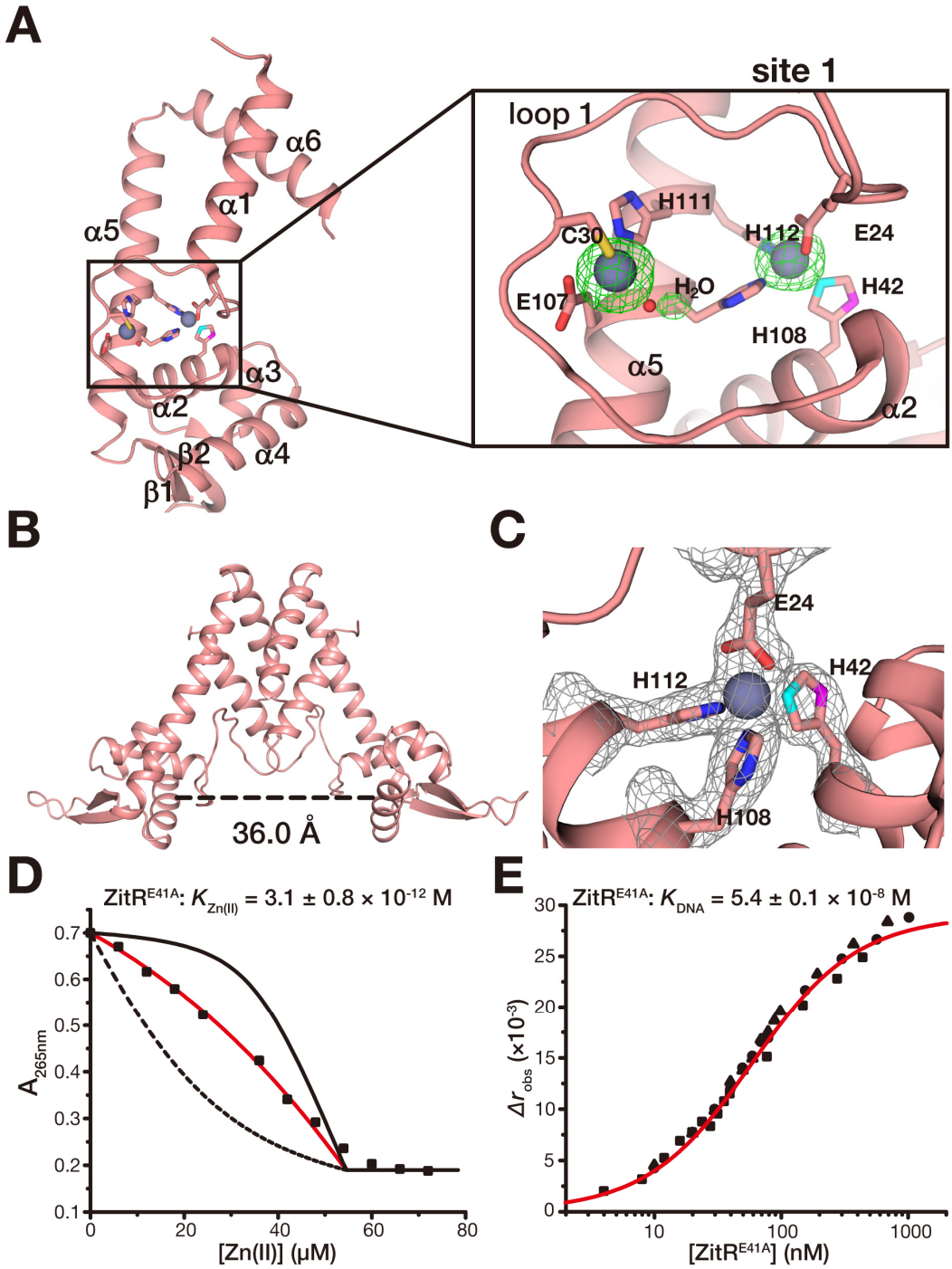

Figure S7. Structural and biochemical characterization of Zn(II)-ZitR^{E41A}. (A) Crystal structure of monomeric Zn(II)-ZitR^{E41A}. Close-up view of the two zinc-binding sites is shown on the right. F_o-F_c omit electron density map of the bound Zn(II) ion (gray sphere) contoured at 3.0σ was displayed as green mesh. **(B)** Structure of dimeric Zn(II)-ZitR^{E41A}. The distance between helix α4 and α4' in dimeric

ZitR was indicated by the dashed line. **(C)** $2F_o$-F_c electron density map of the Zn(II) occupied site 1 of Zn(II)-ZitR^{E41A}. The Nε2 atom on H42 was used for coordination. The map is contoured at 1.0σ and shown as gray mesh. **(D)** Representative binding isotherms of titrating Zn(II) into a mixture of 34.8 μM ZitR^{E41A} monomer and 19.6 μM quin-2. The red solid lines are fitting to a model for 1:1 stoichiometric binding while the black solid and dashed lines are simulated curves with Zn(II) affinities of ZitR proteins 10-fold tighter and weaker than the fitted value, respectively. **(E)** Binding isotherms of titrating ZitR^{E41A} into the fluorescently labeled *zit* promoter DNA. The red solid lines are simulated curves of the mean K_{DNA} values in a 1:1 ZitR dimer:DNA binding model. The *x* axes is plotted on a logarithmic scale. Indicated affinity values are mean ± SEM of three independent experiments (different symbol shapes). Nδ1 and Nε2 of H42 are shown as magenta and cyan respectively for clarity in all panels.

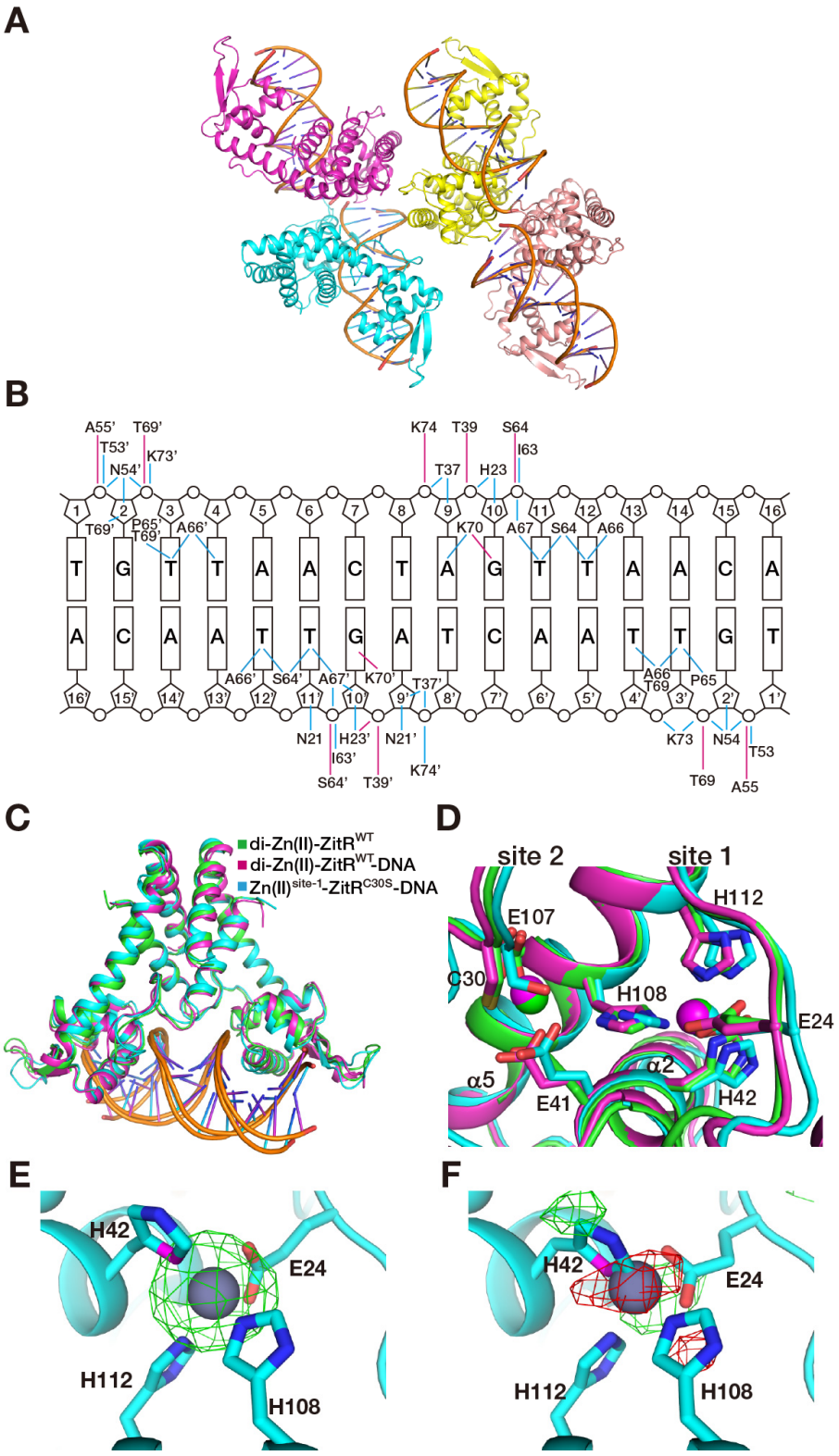

Figure S8. Crystal structure of Zn(II)$^{site\text{-}1}$-ZitR^{C30S}-DNA complex. **(A)** Four separate complexes were found in each asymmetric unit and colored differently. **(B)** Schematic representation of interactions

between ZitR^{C30S} protein and DNA in the structure. Magenta lines indicate direct hydrogen bonds and cyan lines indicate van der Waals interactions. **(C)** Superposition of structures of Zn(II)$^{site-1}$-ZitR^{C30S}-DNA complex (cyan), and di-Zn(II)-ZitR^{WT} with (magenta) and without DNA (green) (rmsd between Zn(II)$^{site-1}$-ZitR^{C30S}-DNA and di-Zn(II)-ZitR^{WT}-DNA: 0.76 Å for 267 Cα atoms; rmsd between Zn(II)$^{site-1}$-ZitR^{C30S}-DNA and di-Zn(II)-ZitR^{WT}: 0.75 Å for 249 Cα atoms). **(D)** Structural comparison of the Zn(II)-binding sites in Zn(II)$^{site-1}$-ZitR^{C30S}-DNA complex (cyan), and di-Zn(II)-ZitR^{WT} with (magenta) and without DNA (green). **(E, F)** F_o-F_c omit electron density map of site 1 modeled with Nδ1-coordinating **(E)** and Nε2-coordinating **(F)** H42 in Zn(II)$^{site-1}$-ZitR^{C30S}-DNA complex, respectively. The positive and negative density around H42 together with the unfavorable geometry of H42 in **(F)**, which are absent in **(E)**, indicate errors in the model of **(F)** and that Nδ1 but not Nε2 is used for coordination of Zn(II) ion (gray sphere) in site 1 of Zn(II)$^{site-1}$-ZitR^{C30S}-DNA complex. Maps are contoured at 3.0σ (green) and -3.0σ (red) respectively. Nδ1 of H42 is shown as magenta for clarity in (E) and (F).

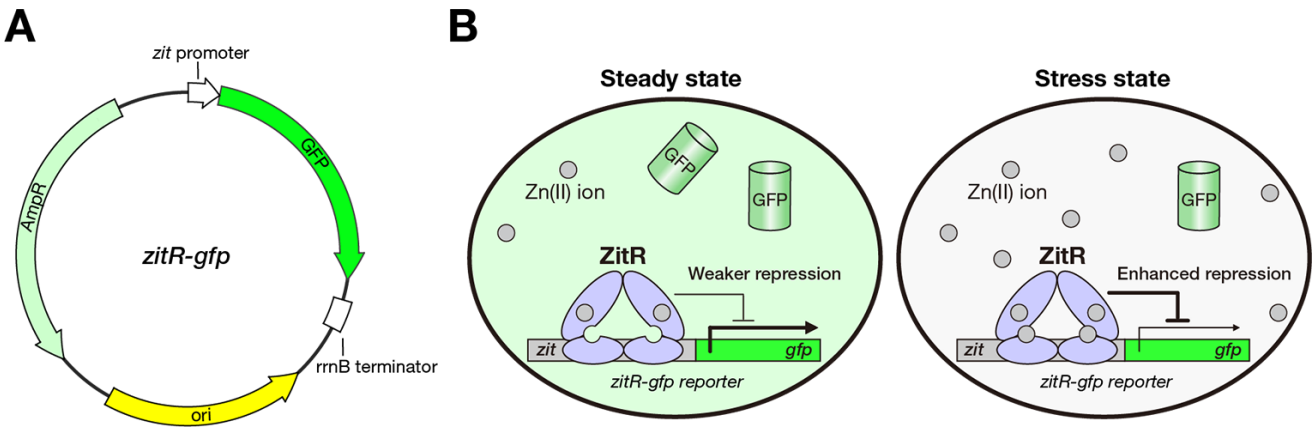

Figure S9. Schematic presentation of measuring transcriptional regulation of ZitR via *zitR-gfp* reporter. (A) Map of the *zitR-gfp* reporter plasmid. The *zitR-gfp* reporter plasmid consists of replication origin, ampicillin resistance gene and *gfp* gene under the control of *zit* promoter. **(B)** Cartoon description for validating ZitR-controlled transcriptional repression of the *zitR-gfp* reporter inside cells. Transcription of *gfp* gene will be repressed by ZitR protein that results in decreased fluorescence

intensity of GFP. This change can be analyzed by flow cytometry on live *E. coli* cells. When cells are under Zn(II) stress conditions, Zn(II) coordination at site 2 would induce ZitR to have enhanced transcriptional repression to the *zitR-gfp* reporter, which results in decreased fluorescence intensity of GFP.

SI TABLES

Table S1: Data collection and refinement statistics of the crystal structures of ZitR variants

	di-Zn(II)-ZitR^{WT}	di-Zn(II)-ZitR^{WT}-DNA	Zn(II)$^{site-1}$-ZitR^{C30S}	Zn(II)$^{site-1}$-ZitR^{C30S}-DNA
Data collection				
Space group	$P2_1$	$P2_1$	$P4_12_12$	$P2_1$
Cell dimensions				
a, *b*, *c* (Å)	34.8, 125.8, 153.7	86.6, 101.6, 101.5	62.2, 62.2, 117.3	89.5, 103.1, 104.9
α, β, γ (°)	90, 91.0, 90	90, 91.1, 90	90, 90, 90	90, 94.2, 90
Resolution (Å)	50.0-2.31 (2.35-2.31)	50.0-2.44 (2.48-2.44)	50.0-1.52 (1.57-1.52)	50.0-2.77 (2.87-2.77)
R_{merge}	0.081 (0.769)	0.127 (0.984)	0.077 (0.973)	0.080 (0.873)
$I/\sigma I$	17.7 (2.0)	11.9 (2.0)	29.2 (2.6)	18.0 (1.9)
Completeness (%)	99.0 (99.5)	98.2 (98.6)	99.8 (100.0)	98.5 (98.4)
Redundancy	3.1 (3.1)	2.9 (2.8)	9.3 (9.6)	3.8 (3.7)
Refinement				
Resolution (Å)	48.66-2.40	40.12-2.60	29.22-1.65	42.49-2.90
R_{merge} in the last shell	0.559	0.527	0.548	0.593
No. reflections	49001	52172	27903	38357
R_{work} / R_{free}	0.221/0.289	0.191/0.247	0.206/0.226	0.205/0.263
No. atoms				
Protein	8954	9190	1152	9083
DNA	0	2600	0	2600
Ligand/ion	16	16	1	8
Water	108	382	212	26
B-factors				
Protein	69.47	49.51	29.10	92.65
DNA	0	42.98	0	70.69
Ligand/ion	57.60	44.64	22.57	80.06
Water	60.17	42.58	38.22	66.98
R.m.s. deviations				
Bond lengths (Å)	0.009	0.008	0.005	0.009
Bond angles (°)	1.145	1.244	0.844	1.328

	Zn(II)-ZitR^{E41A}	ZitR^{C30AH42A}	apo-ZitR^{C30AH42A}
Data collection			
Space group	*C*2	*C*2	$P4_12_12$
Cell dimensions			
a, *b*, *c* (Å)	77.4, 94.2, 31.9	87.0, 86.9, 126.8	61.1, 61.1, 123.7
α, β, γ (°)	90, 110.1, 90	90, 90.7, 90	90, 90, 90
Resolution (Å)	50.0-1.88 (1.95-1.88)	50.0-2.15 (2.19-2.15)	50.0-2.07 (2.14-2.07)
R_{merge}	0.062 (0.622)	0.076 (0.747)	0.066 (0.957)
$I / \sigma I$	19.9 (2.1)	17.3 (2.1)	30.9 (3.1)
Completeness (%)	99.5 (100.0)	97.6 (99.1)	98.7 (100.0)
Redundancy	3.7 (3.8)	3.6 (3.8)	9.1 (9.4)
Refinement			
Resolution (Å)	30.16-1.90	19.55-2.30	27.58-2.20
R_{merge} in the last shell	0.651	0.383	0.571
No. reflections	15905	39696	12078
R_{work} / R_{free}	0.220/0.255	0.251/0.301	0.258/0.269
No. atoms			
Protein	1148	4584	1037
Ligand/ion	21	4	0
Water	73	96	21
B-factors			
Protein	46.10	63.59	59.62
Ligand/ion	48.54	60.88	0
Water	48.17	63.12	57.12
R.m.s. deviations			
Bond lengths (Å)	0.020	0.008	0.008
Bond angles (°)	1.857	1.083	0.903

*Numbers in parentheses represent statistics in highest resolution shell.

Table S2: Structural information of ZitR protein on zinc coordination sites and distance between helices α4/α4' (calculated from distance between Cα atoms of A71 and A71')

ZitR variants	No. of Zn per monomer		Residues for site-1	Residues for site-2	Distance between helices α4/α4'* (Å)
	By ICP-MS	In crystal			
$ZitR^{WT}$	1.68 EDTA treated: 0.02	2	H108, H112, H42, E24	C30, E41, E107, H_2O	30.1
$ZitR^{WT}$-DNA	-	2	H108, H112, H42, E24	C30, E41, E107, H_2O	28.0
$ZitR^{C30S}$	1.01	1	H108, H112, H42, E24	-	41.9
$ZitR^{C30S}$-DNA	-	1	H108, H112, H42, E24	-	28.0
$ZitR^{E41A}$	2.02	2	H108, H112, H42, E24	C30, H111, E107, H_2O	36.0
$ZitR^{C30AH42A}$	1.34	1	H108, H112, E41, E24	-	45.4
apo-$ZitR^{C30AH42A}$	-	0	-	-	43.6

*For structures contain more than one subunit in an asymmetric units, average values of all subunits are listed.

Table S3: Conditions for crystallization of ZitR variants

ZitR Variants	Optimized conditions for crystal growth
di-Zn(II)-ZitR^{WT}	0.05 M Magnesium chloride hexahydrate, 0.1 M HEPES pH 7.5, 30% v/v Polyethylene glycol monomethyl ether 550
di-Zn(II)-ZitR^{WT} -DNA	0.1 M Sodium cacodylate pH 6.1, 0.05 M Magnesium chloride hexahydrate, 0.1 M Sodium chloride, 20% w/v Polyethylene glycol 4000
Zn(II)$^{site-1}$-ZitR^{C30S}	0.19 mM CYMAL®-7, 0.1 M HEPES pH 7.5, 40% v/v Polyethylene glycol 400
Zn(II)$^{site-1}$-ZitR^{C30S}-DNA	0.1 M Sodium cacodylate pH 6.1, 0.05 M Magnesium chloride hexahydrate, 0.1 M Sodium chloride, 20% w/v Polyethylene glycol 4000
Zn(II)-ZitR^{E41A}	0.05 M Calcium chloride dihydrate, 0.1 M MES monohydrate pH 6.0, 45% v/v Polyethylene glycol 200
ZitR^{C30AH42A}	0.1 M HEPES pH 7.5, 42% v/v Polyethylene glycol 200
apo-ZitR^{C30AH42A}	0.1 M HEPES pH 7.5, 63% v/v Polyethylene glycol 200, 10 mM EDTA

Table S4: Oligonucleotides used in this study

	Forward Primer (5'-3')	Reverse Primer (5'-3')
For site-directed mutagenesis		
ZitR^{C30S}	ACACGAAATCCTGCTGGGC AAAAGCGA	AGTTTAACATCACTTTCGCT TTTGCCCAGCA
ZitR^{C30A}	ACACGAAATCCTGCTGGGC AAAGCGGA	AGTTTAACATCACTTTCCGC TTTGCCCAGCA
ZitR^{E41A}	GTGATGTTAAACTGACCTC CACGCAGGCG	GCAGCATCAGGATATGCGC CTGCGTGGAG
ZitR^{H42A}	GTTAAACTGACCTCCACGC AGGAAGCG	CAGCAGCATCAGGATCGCTT CCTGCGTGGA
ZitR$^{H42\delta meH}$	GTTAAACTGACCTCCACGC AGGAATAG	CAGCAGCATCAGGATCTATT CCTGCGTGGA